# Supplementary Information

## *In situ* activation of flexible magnetoelectric membrane enhances bone defect repair

Wenwen Liu[1], Han Zhao[1], Chenguang Zhang[2], Shiqi Xu[3], Fengyi Zhang[4], Ling Wei[5], Fangyu Zhu[1], Ying Chen[6], Yumin Chen[1], Ying Huang[1], Mingming Xu[1], Ying He[1], Boon Chin Heng[7], Jinxing Zhang[8], Yang Shen[9], Xuehui Zhang[10]*, Houbing Huang[2]*, Lili Chen[11]* and Xuliang Deng[1]*

These authors contributed equally: Wenwen Liu, Han Zhao, Chenguang Zhang.

**Affiliations**

[1] Department of Geriatric Dentistry, Peking University School and Hospital of Stomatology, Beijing, P. R. China

[2] Hospital of Stomatology, Guanghua School of Stomatology, Sun Yat-sen University, Guangzhou, P. R. China

[3] School of Materials Science and Engineering & Advanced Research, Institute of Multidisciplinary Science, Beijing Institute of Technology, Beijing, P. R. China

[4] Department of Orthopedics, The Second Xiangya Hospital, Central South University, Changsha, P. R. China

[5] Third Clinical Division, Peking University School and Hospital of Stomatology, Beijing, P. R. China

[6] Department of Prosthodontics, The First Clinical Division, Peking University School and Hospital of Stomatology, Beijing, P. R. China

[7] Central Laboratory, Peking University School and Hospital of Stomatology, Beijing, P. R. China

[8] Department of Physics, Beijing Normal University, Beijing, P. R. China

[9] State Key Laboratory of New Ceramics and Fine Processing Department of Materials Science and Engineering Tsinghua University, Beijing, P. R. China

[10] Department of Dental Materials & Dental Medical Devices Testing Center, Peking University School and Hospital of Stomatology, Beijing 100081, PR China.

[11] Department of Stomatology, Union Hospital, Tongji Medical College, Huazhong University of Science and Technology, Wuhan, P. R. China

**Corresponding authors**

Correspondence to Xuehui Zhang, Houbing Huang, Lili Chen, or Xuliang Deng.

*Emails: zhangxuehui@bjmu.edu.cn; hbhuang@bit.edu.cn; lily-c1030@163.com; kqdengxuliang@bjmu.edu.cn

# Table of Contents

**Supplementary Figure 1-19**.....**3**

**Supplementary Table 1-2**.....**22**

**Supplementary References** .....**24**

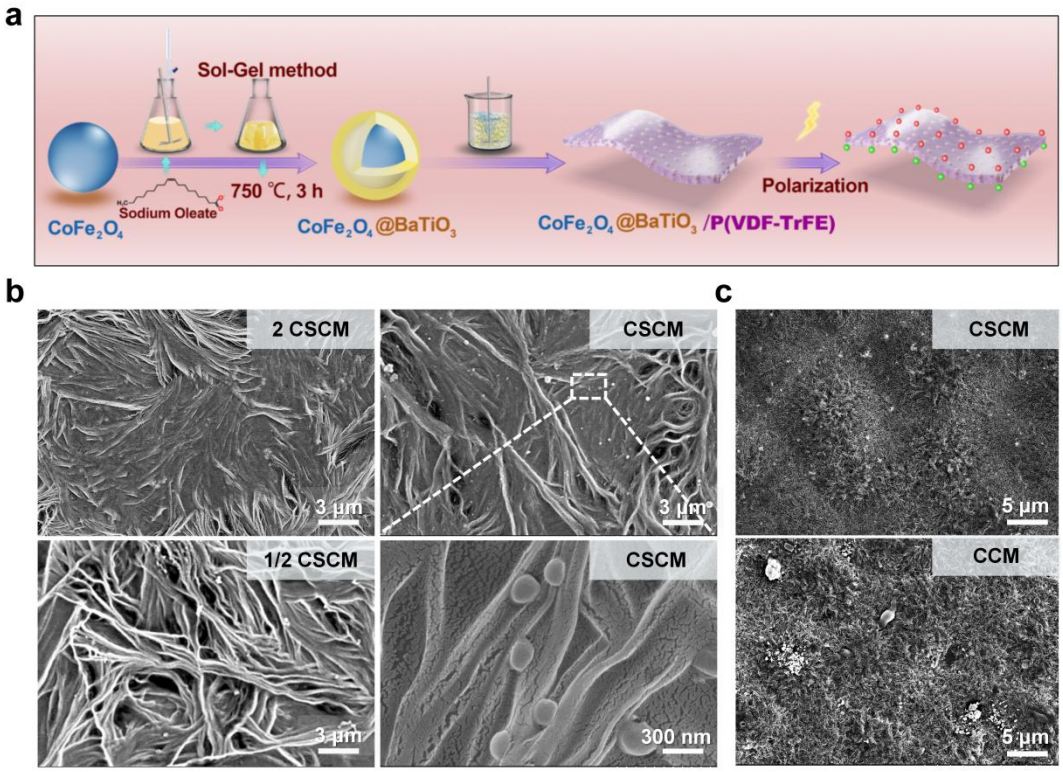


**Supplementary Fig. 1 The fabrication process and characterization of the basic properties of composite membranes.**

**a,** Fabrication process of CFO@BTO core-shell particles and CFO@BTO/P(VDF-TrFE) membrane. **b,** SEM images of 2 CSCM, CSCM and 1/2 CSCM. An enlarged view of the interior of CSCM is shown at the lower right. **c,** SEM images of the surface of CSCM and CCM. At least three times of experiments were repeated independently.

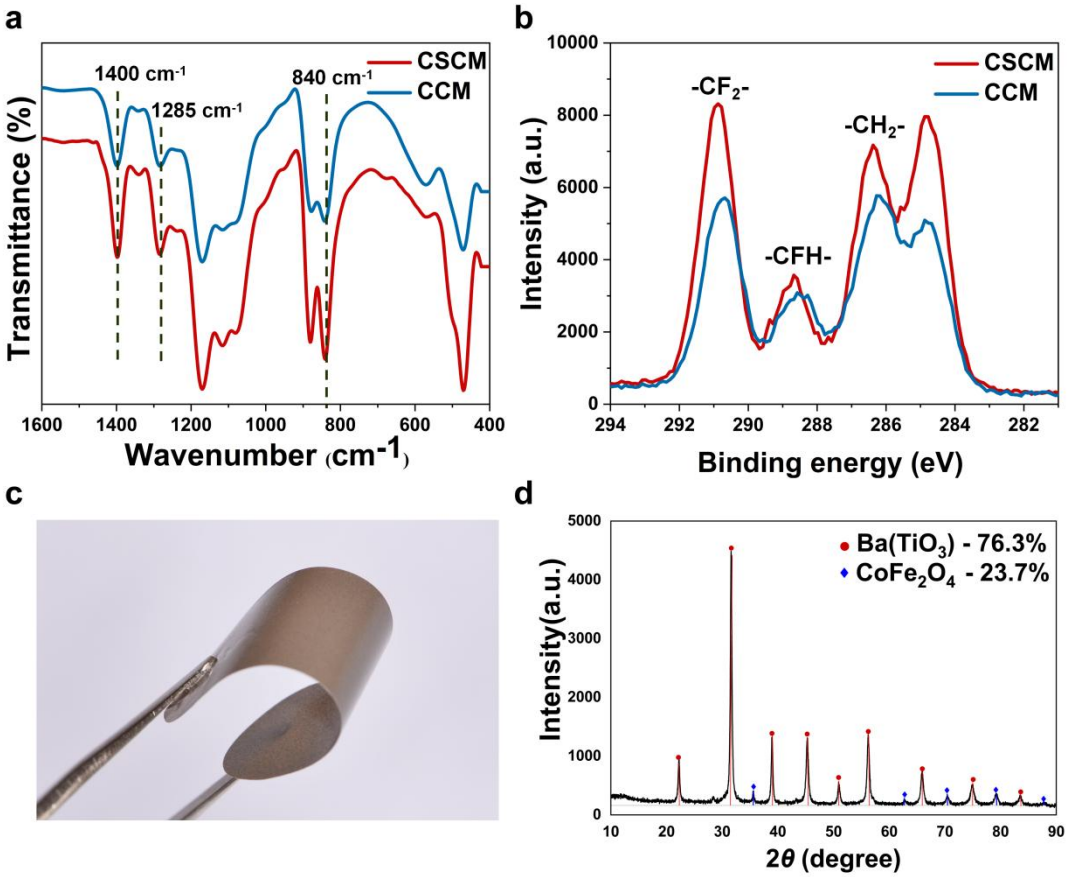


**Supplementary Fig. 2 Characterization of the basic properties of composite membranes.**

**a,** FTIR results of CSCM and CCM. **b,** XPS results for CSCM and CCM. (CSCM represents a composite membrane containing 10% CFO@BTO core-shell particles by weight; 2 CSCM means that the weight content of the core-shell particles is 20%, twice that of CSCM; 1/2 CSCM means 5% core-shell particle weight content, which is half that of CSCM). **c,** Image of CFO@BTO/P(VDF-TrFE) membrane (CSCM). **d,** XRD results of CFO@BTO core-shell. Source data are provided as a Source Data file.

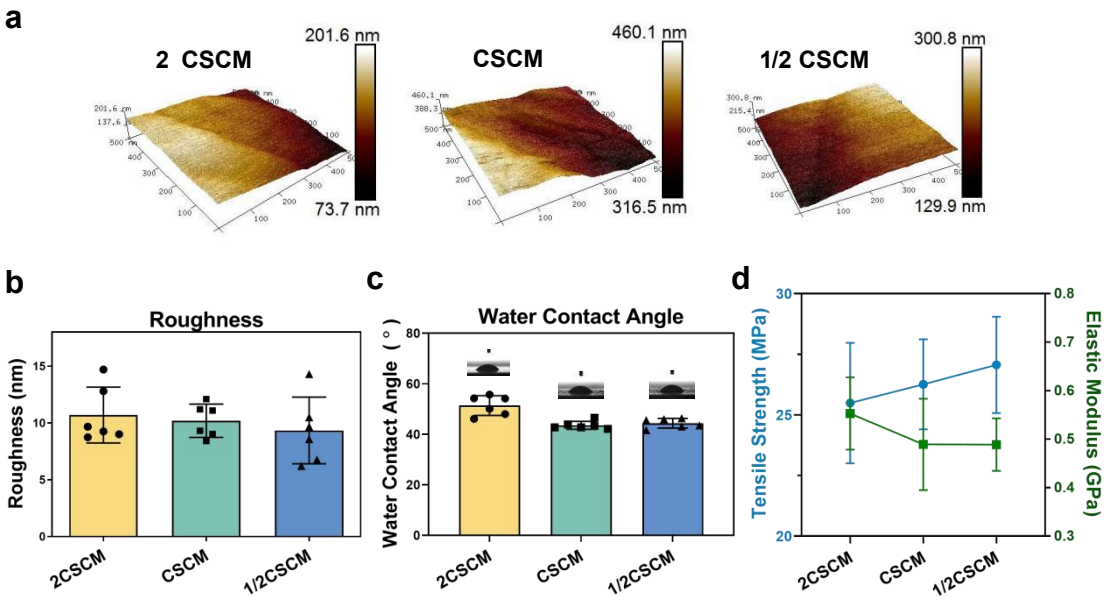


**Supplementary Fig. 3 Surface characteristics and mechanical properties of composite membranes.**

**a,** Surface topography and roughness **(b)** measured by AFM of 2 CSCM, CSCM and 1/2 CSCM.There was no difference in surface roughness between the different membrane groups. *n*=6 independent membrane samples; mean±SEM. **c,** Data statistics and photos of water contact angle, which also showed no significant differences. The contact angle values were 80°±, indicating similar hydrophilicity. *n*=6 independent membrane samples; mean±SEM. **d,** Tensile strength and elastic modulus of 2 CSCM, CSCM and 1/2 CSCM. *n*=6 independent membrane samples; mean±SEM. Source data are provided as a Source Data file.

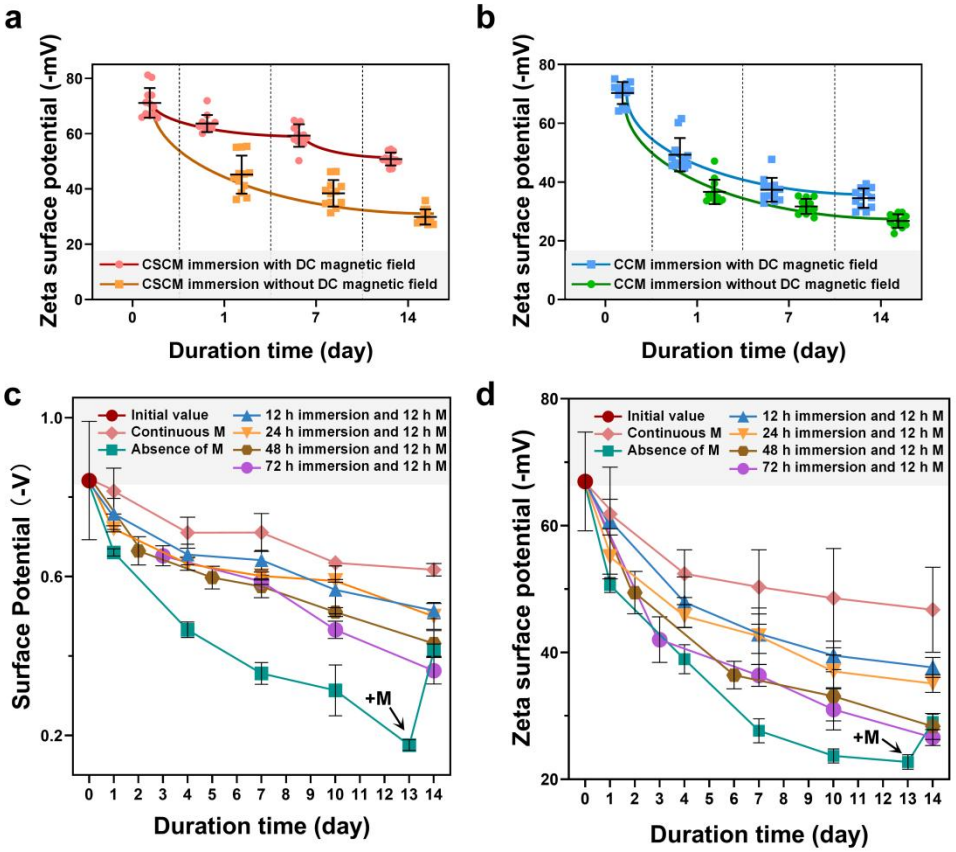


**Supplementary Fig. 4 Characterization of the electrical properties of magnetoelectric composite membranes.**

**a,b,** Zeta potential of CSCM **(a)** and CCM **(b)** immersed in phosphate buffer solution (PBS), with or without exposure to a remote DC magnetic field after 1, 7, 14 days. *n*=12 membranes for per group and per time point; mean±SEM. **c,** Surface potential measured by SKPM and **(d)** zeta potential of CSCM under a continuous magnetic field, 12 h immersion and 12 h magnetic field, 24 h immersion and 12 h magnetic field, 48 h immersion and 12 h magnetic field, 72 h immersion and 12 h magnetic field, and without magnetic field. On the 13$^{th}$ day, a magnetic field was applied to the non-magnetic field exposed group, to observe its reactivation effect on the surface potential. *n*=6 membranes for per group and per time point; mean±SEM. Source data are provided as a Source Data file.

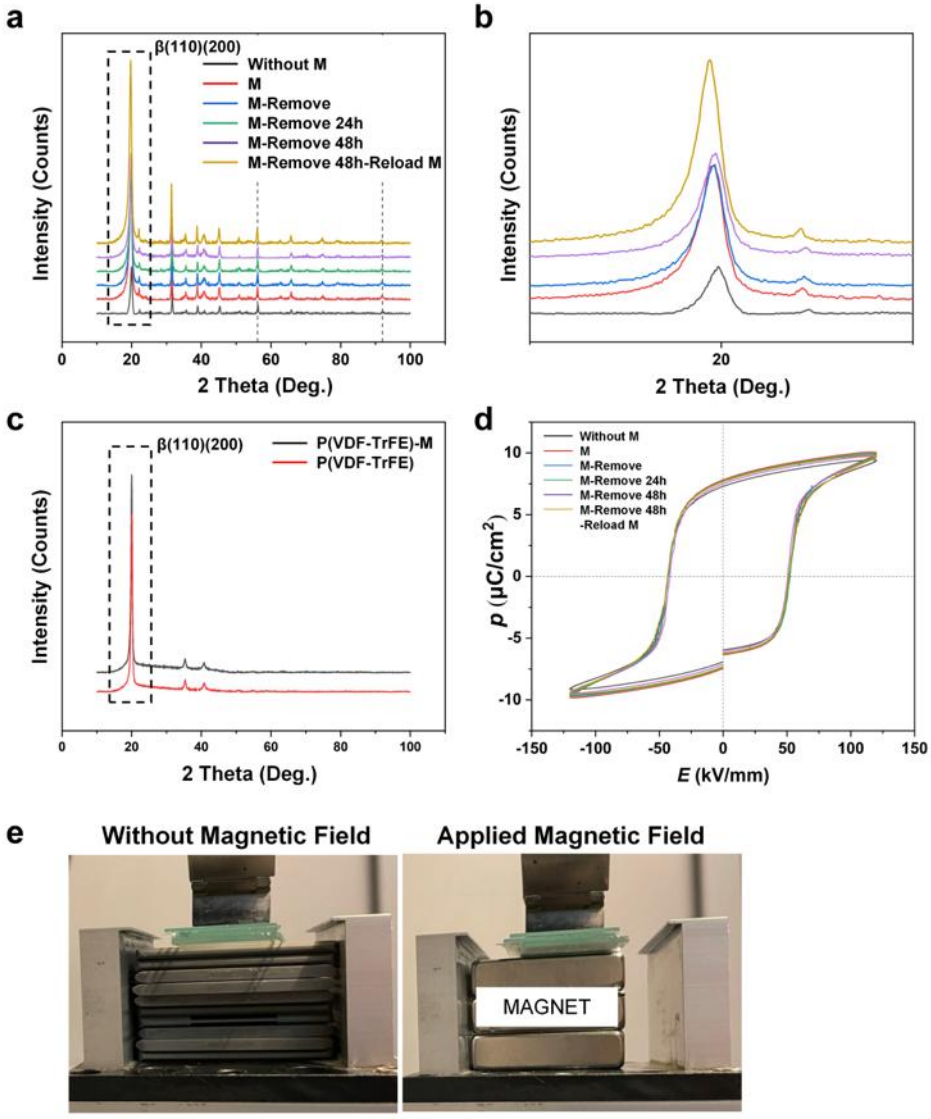


**Supplementary Fig. 5 Phase change detection results and device photos.**

**a,** The XRD results of CSCM under different conditions (without magnetic field, applied magnetic field, magnet removal and 24, 48 h after removing magnet and finally reloading magnetic field). **b,** An enlarged view of figure (a), showing the location of the β-phase. According to Bragg Law $\lambda$=2d • sin$\theta$， the interplanar crystal spacing of CSCM increased after the magnetic field loading. **c,** The XRD results of P(VDF-TrFE) without magnetic field (black line) and applied magnetic field (red line), which showed no shift of the β-phase position. **d,** The electric hysteresis loop of CSCM under different conditions. **e,** Pictures of the device for XRD detection. Source data are provided as a Source Data file.

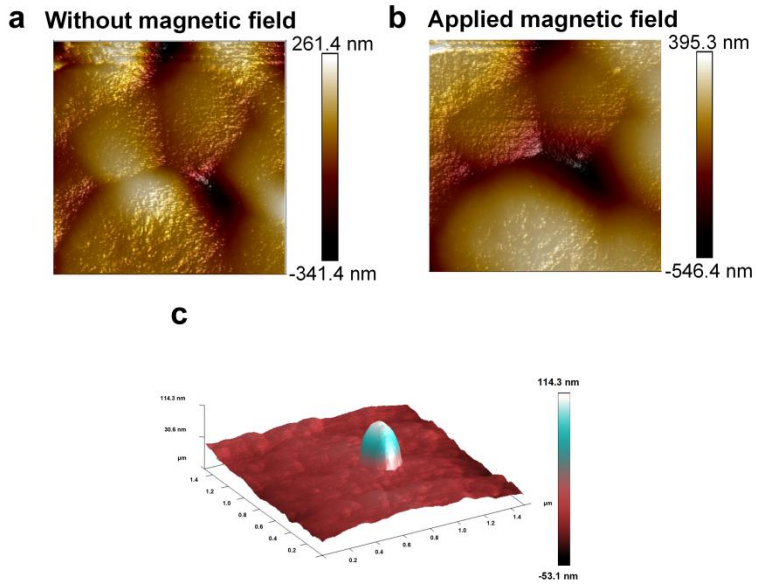


**Supplementary Fig. 6 Morphologies of surface potential and interfacial polarization detection**

**a,** The topography shows the instant change of surface potential before and after applying magnetic field *in situ* **(b)**. **c,** 3D topography image of detecting the interface polarization.

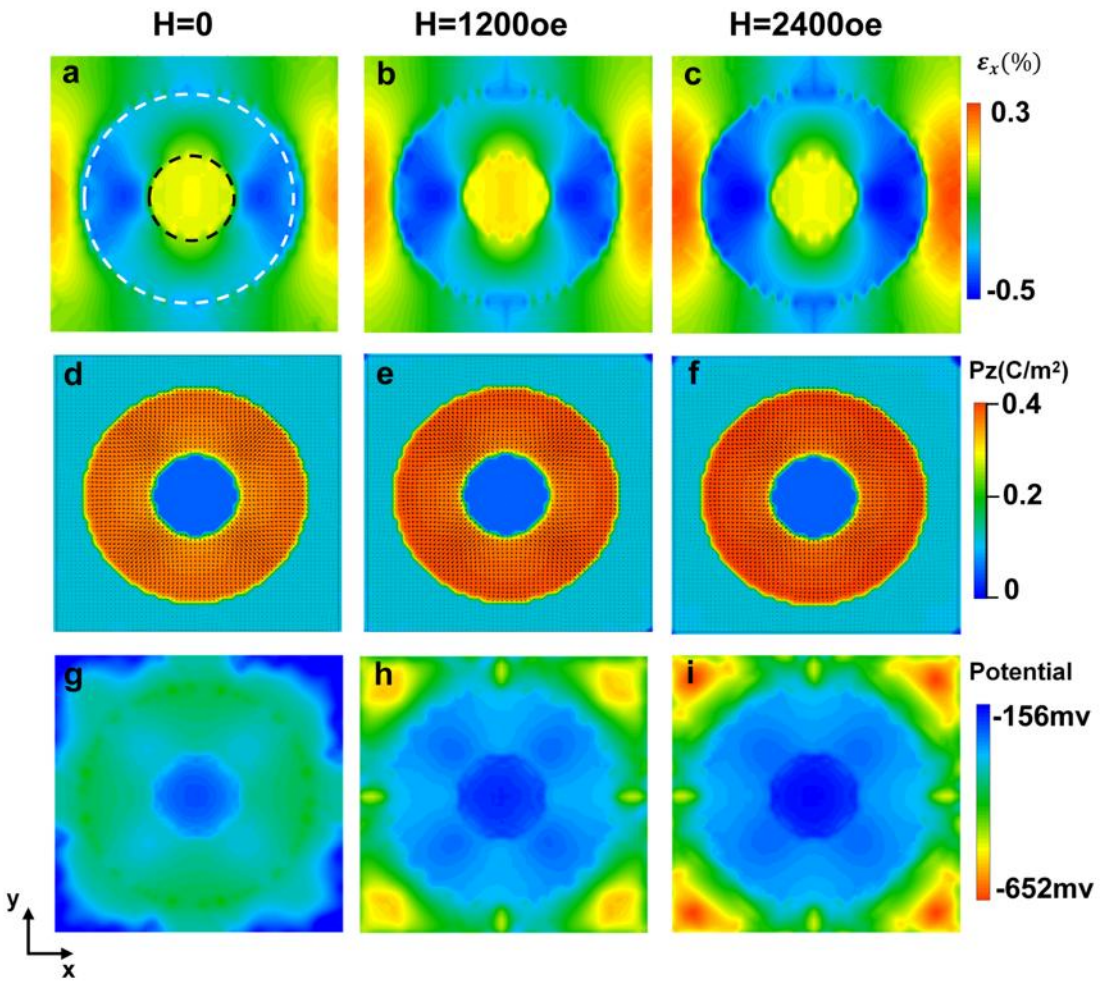


**Supplementary Fig. 7 Phase-field simulation** of the strain distributions along the x-direction under different magnetic fields **(a)** H=0 **(b)** H=1200 Oe **(c)** H=2400 Oe. The polarization component $P_z$ distributions under different magnetic fields **(d)** H=0 **(e)** H=1200 Oe **(f)** H=2400 Oe. The electrical potential distributions under different magnetic fields **(g)** H=0 **(h)** H=1200 Oe **(i)** H=2400 Oe.

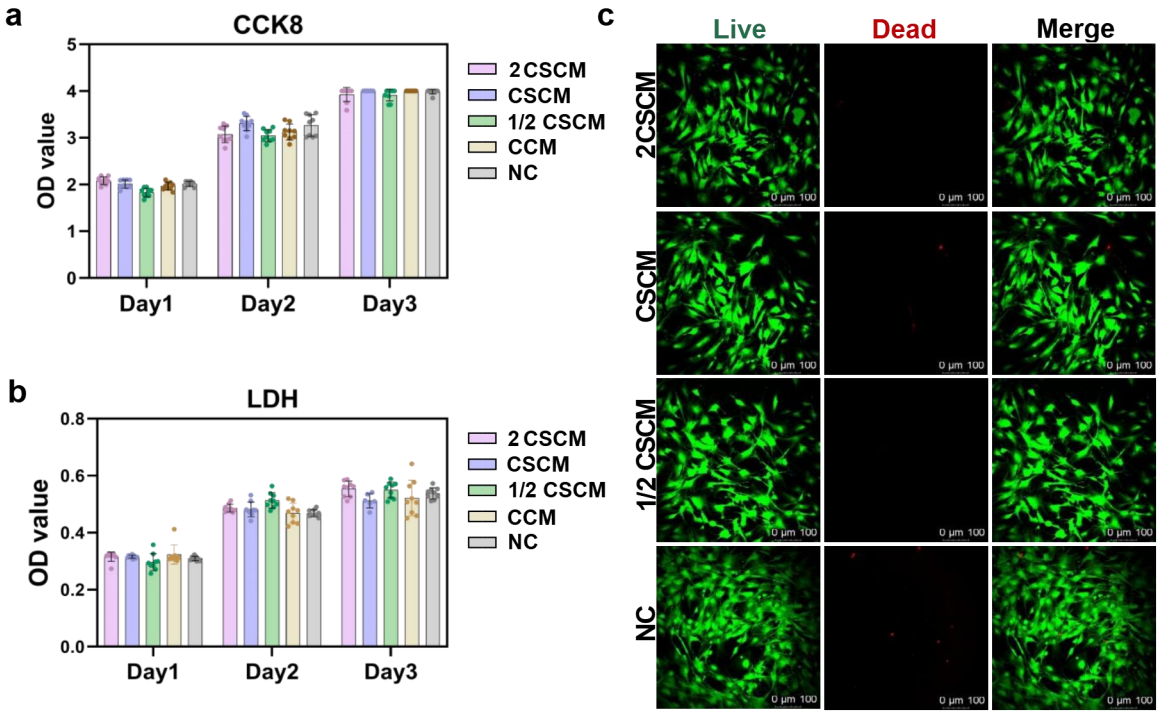


**Supplementary Fig. 8 Biocompatibility of composite membranes in the various groups.**

**a,** Cell proliferation of BM-MSCs cultured on the membranes of various groups by the CCK-8 assay after 1, 2 and 3 days. *n*=9 biologically independent samples; mean±SEM; one-way ANOVA. **b,** The lactate dehydrogenase content in the supernatants of BM-MSCs cultured on the membranes after 1, 2 and 3 days. **c,** Live and dead cell staining on the membranes of different groups. *n*=9 biologically independent samples; mean±SEM; one-way ANOVA. Source data are provided as a Source Data file.

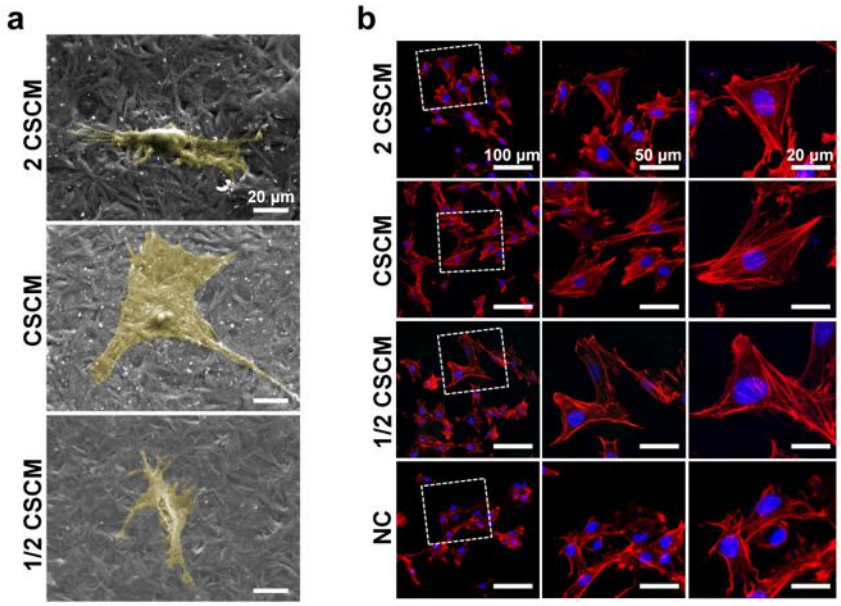


**Supplementary Fig. 9 Characterization of cell spreading on the membrane surfaces.**

**a,** SEM and immunofluorescence images **(b)** of cell spreading on the different membrane groups. At least three times of experiments were repeated independently.

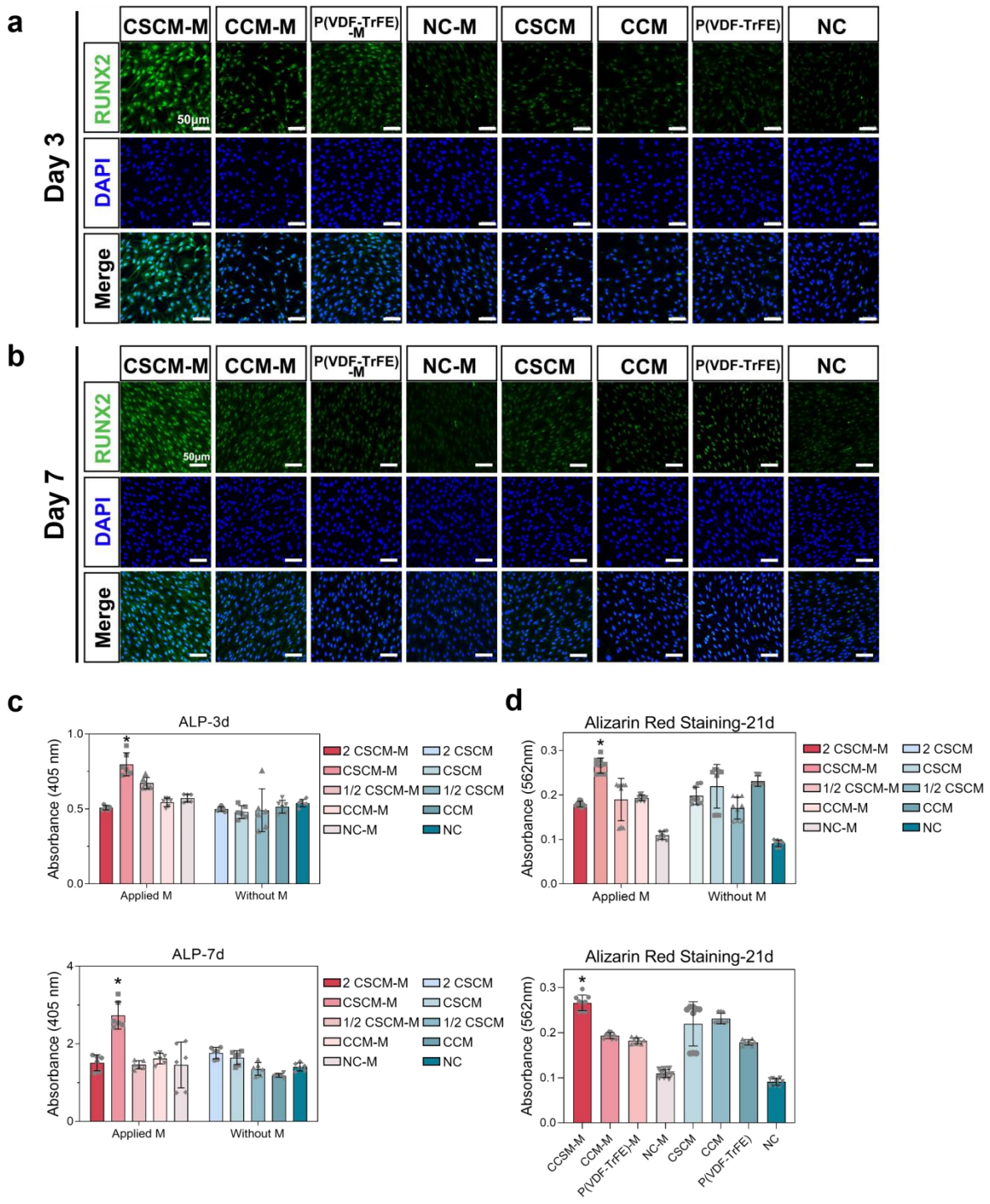


**Supplementary Fig. 10 Osteogenic properties of core-shell magnetoelectric composite membranes**

**a,b,** Immunofluorescence images showed the upregulated expression of RUNX2 in the CSCM-M group after 3 and 7 days of cell culture (Scale bars: 50 μm). **c,** ALP activity after 3 and 7 days of cell culture. *n*=9 biologically independent samples; mean±SEM. *P<0.05, one-way ANOVA. **d,** Quantification of Alizarin red staining after 21 days of cell culture. *n*=9 biologically independent samples; mean±SEM. *P<0.05, one-way ANOVA. Source data are provided as a Source Data file.

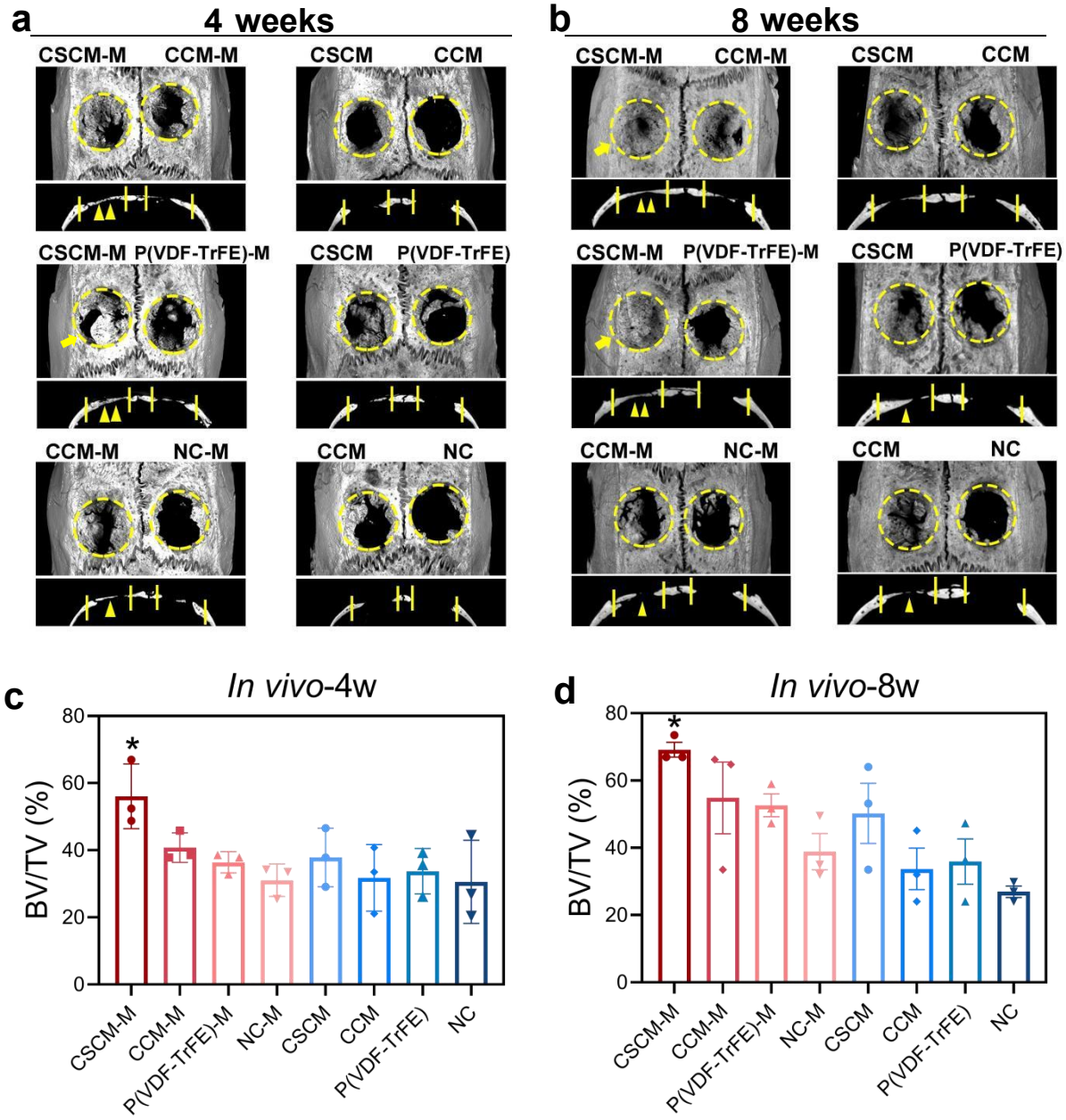


**Supplementary Fig. 11 | Osteogenic properties of core-shell magnetoelectric composite membranes *in vivo*.**

**a,b,** Micro-CT images of bone regeneration in rat cranial defects at 4 **(a)** and 8 **(b)** weeks after membrane implantation, showing the most abundant new bone formation in the CSCM-M group. (Yellow arrows indicated enhanced bone regeneration in the CSCM-M group. Yellow triangles denote the new bone. Yellow dotted lines denote the boundary between nascent bone and host bone.) **c,d,** Quantitative statistics of new bone from Micro-CT analysis. $n$=3 rats for per group and per time point; mean±SEM. *P<0.05, one-way ANOVA. Source data are provided as a Source Data file.

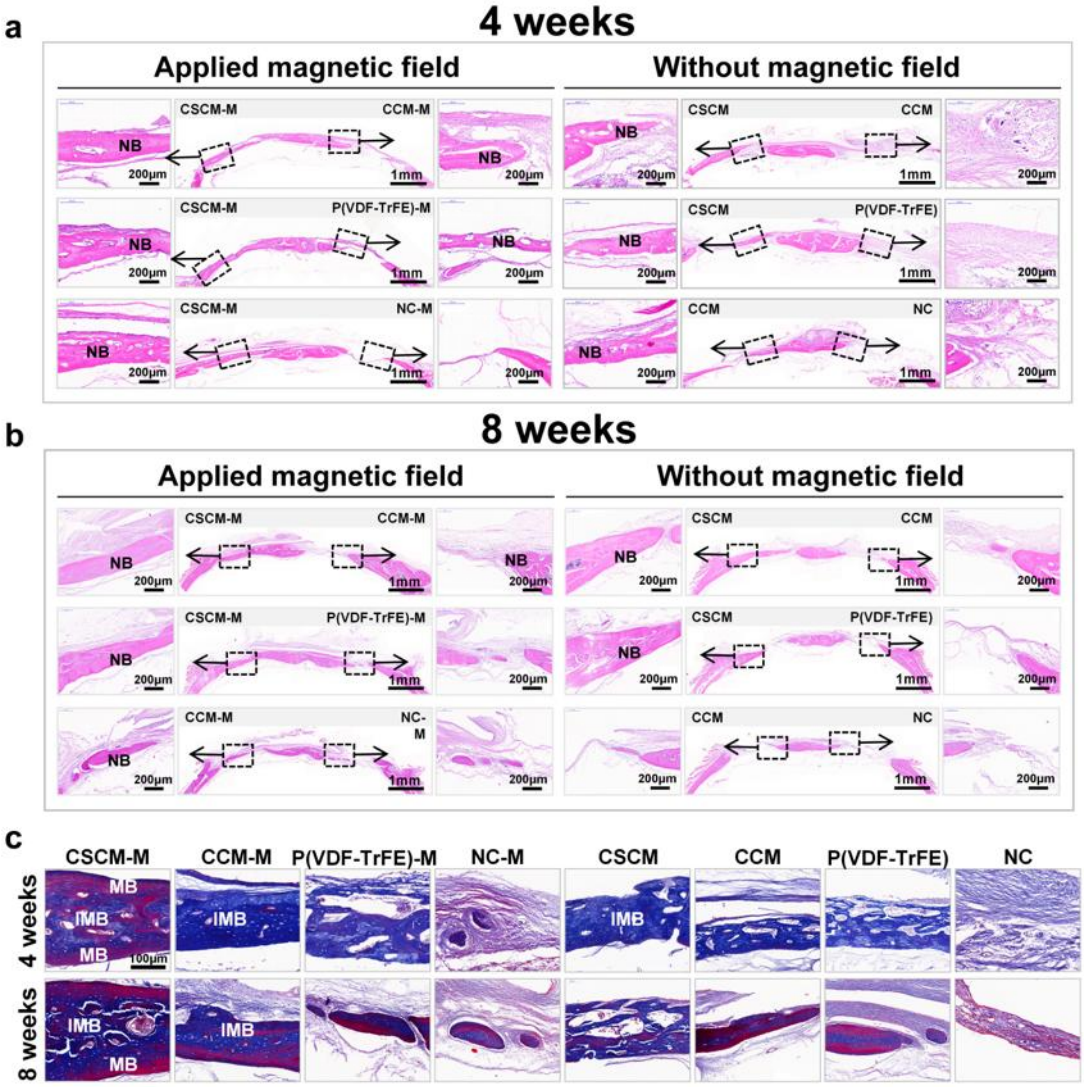


**Supplementary Fig. 12 | Osteogenic properties of core-shell magnetoelectric composite membranes *in vivo***

**a,b,** H&E staining (NB: nascent bone) at 4, 8 weeks after implantation. **c,** Masson's trichrome staining (MB: mature bone; IMB: immature bone). At least three times of experiments were repeated independently.

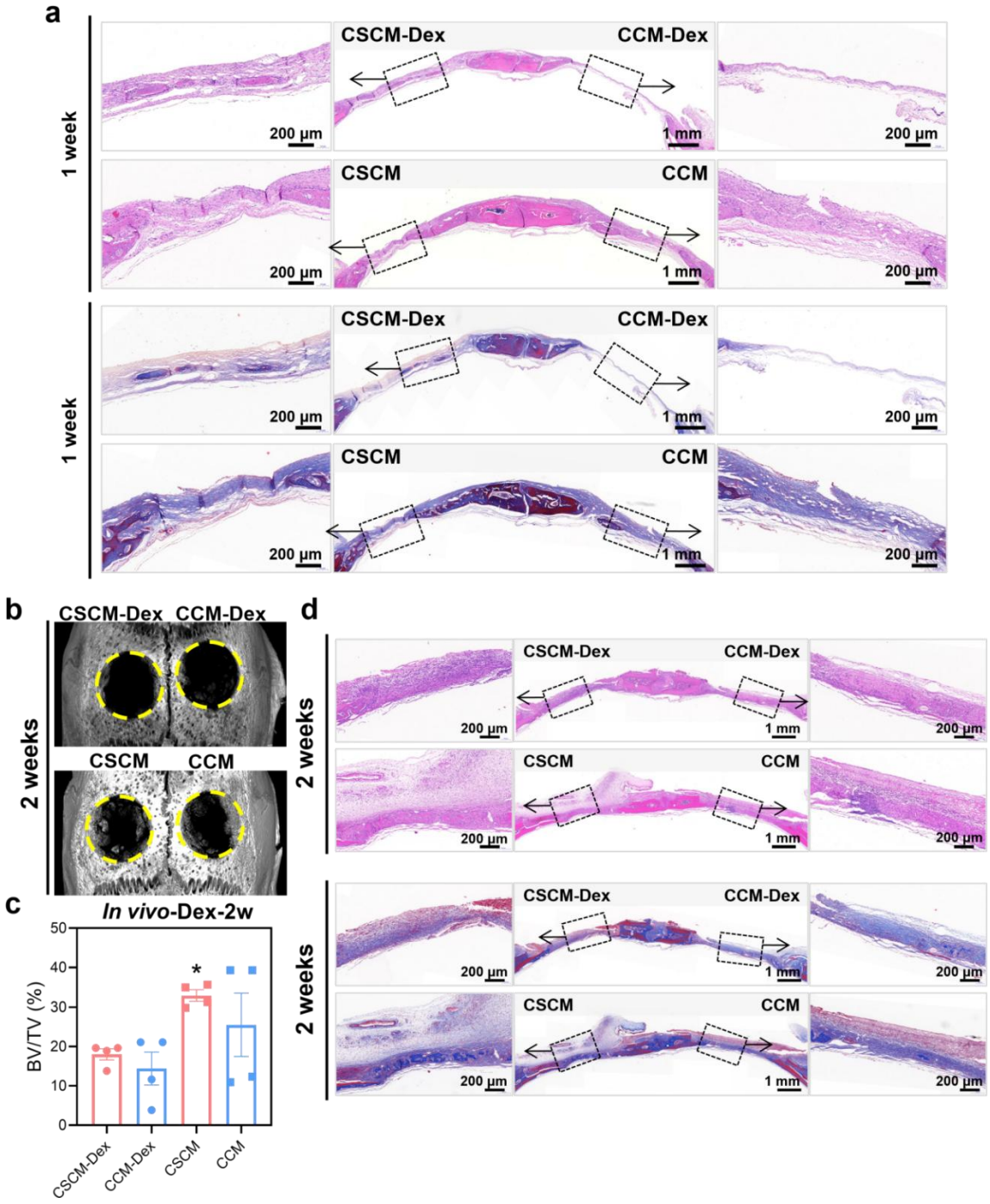


**Supplementary Fig. 13 | Osteogenic inhibition by high dose dexamethasone *in vivo*.**

**a,** H&E staining and Masson's trichrome staining at 1 week, after 3 days implantation and dexamethasone injection. **b,** Micro-CT images of bone regeneration in rat cranial defects at 2 weeks after 3 days of membrane implantation and dexamethasone injection. **c,** Quantitative statistics of new bone from micro-CT analysis. *n*=4 rats for per group and per time point; mean±SEM.*P<0.05, one-way ANOVA. **d,** H&E staining and Masson's trichrome staining at 1 week after 3 days implantation and dexamethasone injection. At least three times of experiments were repeated independently. Source data are provided as a Source Data file.

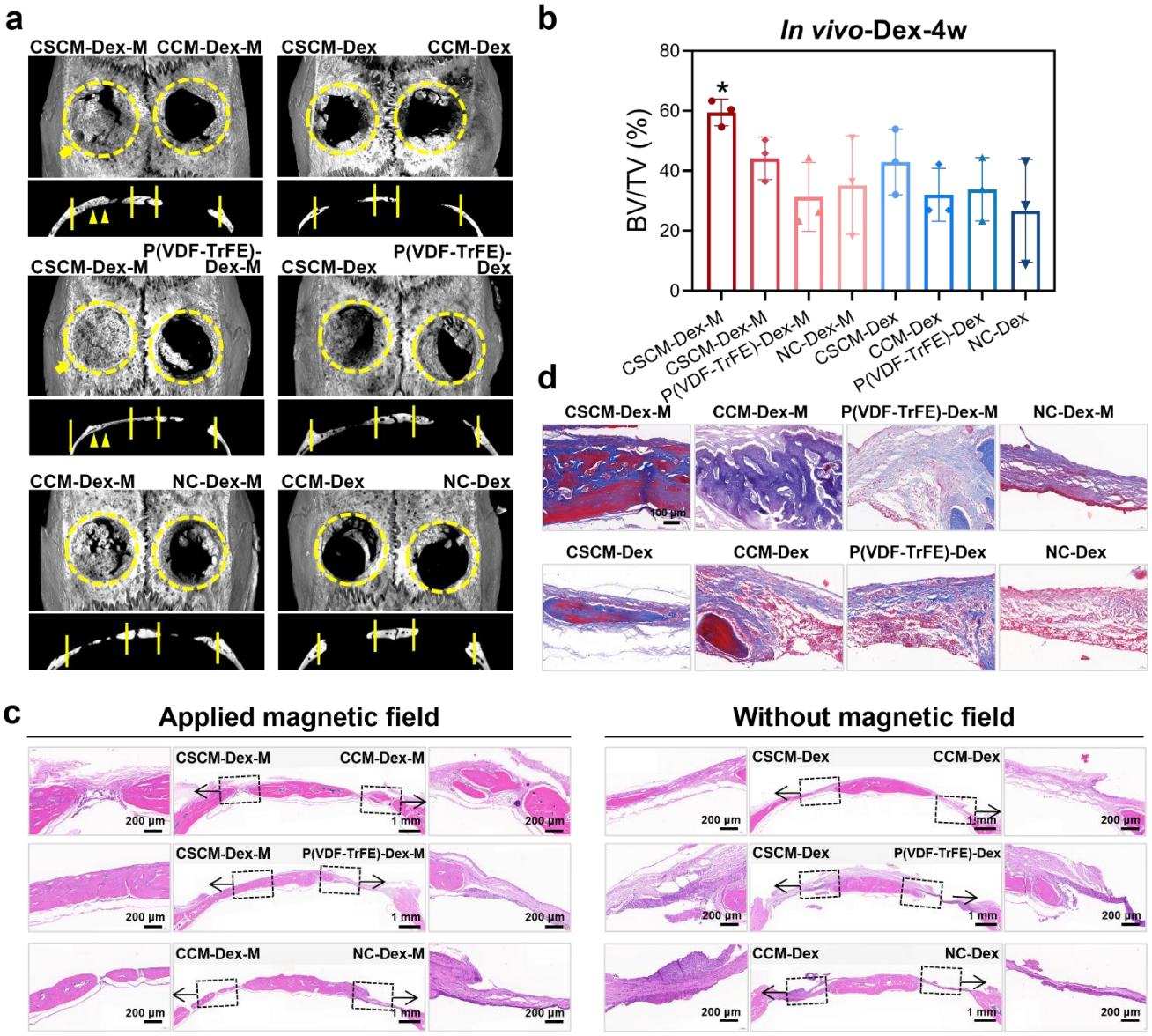


**Supplementary Fig. 14 | The reactivation effect of the implanted core-shell magnetoelectric composite membrane *in vivo* within the rat skull defect model with osteogenesis inhibition.**

**a,** Micro CT images and quantitative statistics **(b)** of bone volume after dexamethasone (Dex) injection to inhibit osteogenesis with and without magnetic treatment (4 weeks). *n*=3 rats for per group; mean±SEM. *P<0.05, one-way ANOVA. **c,** H&E staining and Masson's trichrome staining **(d)** of new bone formation after dexamethasone (Dex) injection to inhibit osteogenesis with and without magnetic treatment (4 weeks). Source data are provided as a Source Data file. At least three times of experiments were repeated independently.

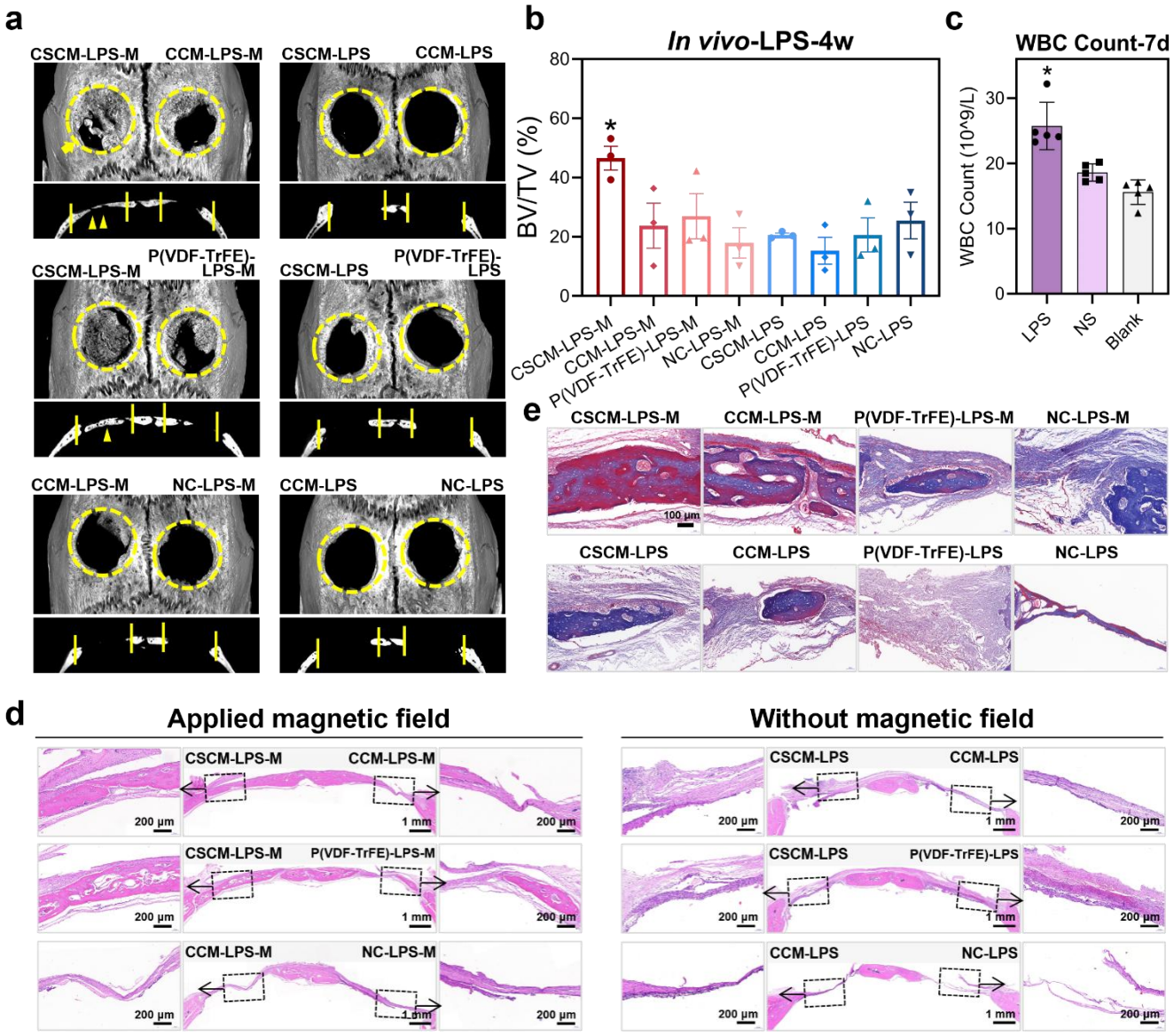


**Supplementary Fig. 15 | The reactivation effect of implanted core-shell magnetoelectric composite membrane *in vivo* within the rat skull defect model with LPS-induced systemic inflammation.**

**a,** Micro CT images and quantitative statistics **(b)** of bone volume after LPS injection to induce systemic inflammation with and without magnetic treatment (4 weeks). *n*=3 rats for per group; mean±SEM. *P<0.05, one-way ANOVA. **c,** White blood cell count at 7 d after membrane implantation. (LPS-1 mg/kg LPS injection, NS-normal saline injection, Blank-without any injection). *n*=5 rats for per group; mean±SEM. *P<0.05, one-way ANOVA. **d,** H&E staining and Masson's trichrome staining **(e)** of new bone formation after LPS injection to induce systemic inflammation with and without magnetic treatment (4 weeks). Source data are provided as a Source Data file. At least three times of experiments were repeated independently.

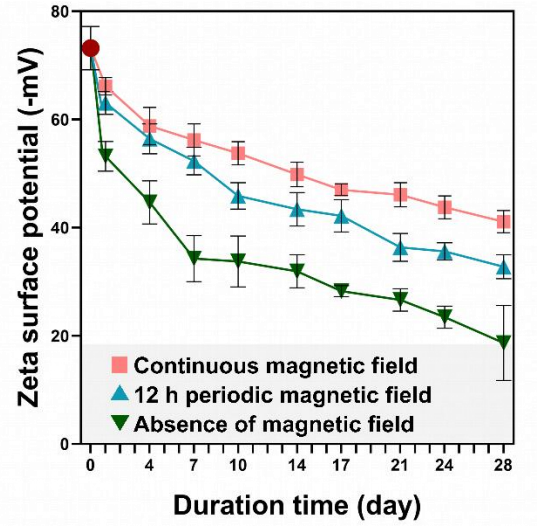


**Supplementary Fig. 16 The surface potentials of the membranes immersed in culture medium decreased over time.** *n*=6 independent membrane samples for per group and per time point; mean±SEM. Source data are provided as a Source Data file.

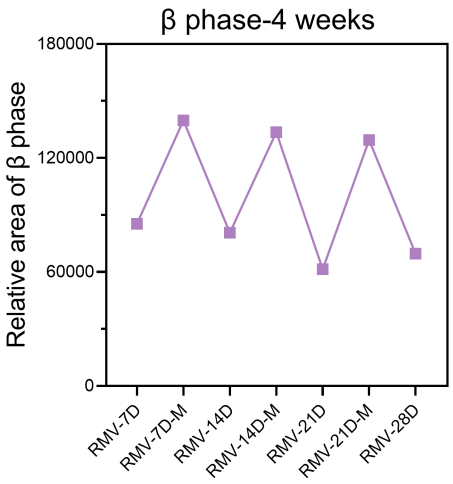


**Supplementary Fig. 17 Relative area of β -phase calculated from XRD.** The β -phase transition was detected from day 7 to day 28 after the magnetic field was removed and 3 cycles were performed. Source data are provided as a Source Data file.

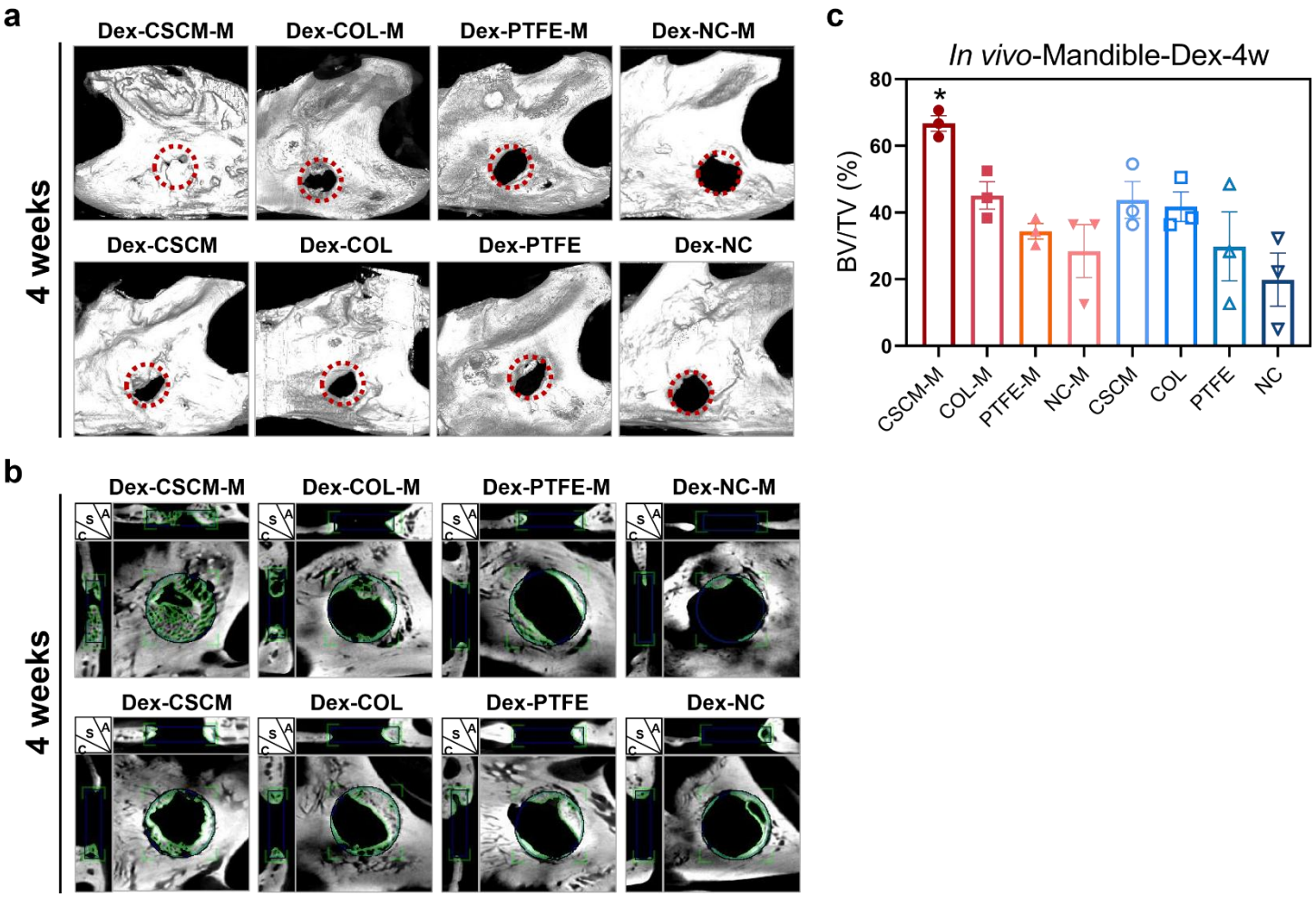


**Supplementary Fig. 18 Comparison of osteogenic effects of CSCM versus commercially-available membranes in promoting bone defect repair.** The model of mandibular critical defect (3 mm) combined with Dex-induced osteogenic inhibition in rats were used in this study. **a,** Three-dimensional micro-CT images at four weeks after material implantation, with and without magnetic field treatment (4 weeks). The bone defect areas are marked by a red dotted circle. **b,** Two-dimensional images of the defect areas at 4 weeks after material implantation and co-morbidity model preparation. The bone defect areas are marked by circles or rectangles. S=Sagittal plane, C=Coronal plane, A=Cross section. **c,** Quantitative statistics of the ratio of new bone volume to total volume (BV/TV). *n*=3 rats for per group; mean±SEM. *P<0.05, one-way ANOVA. Source data are provided as a Source Data file.

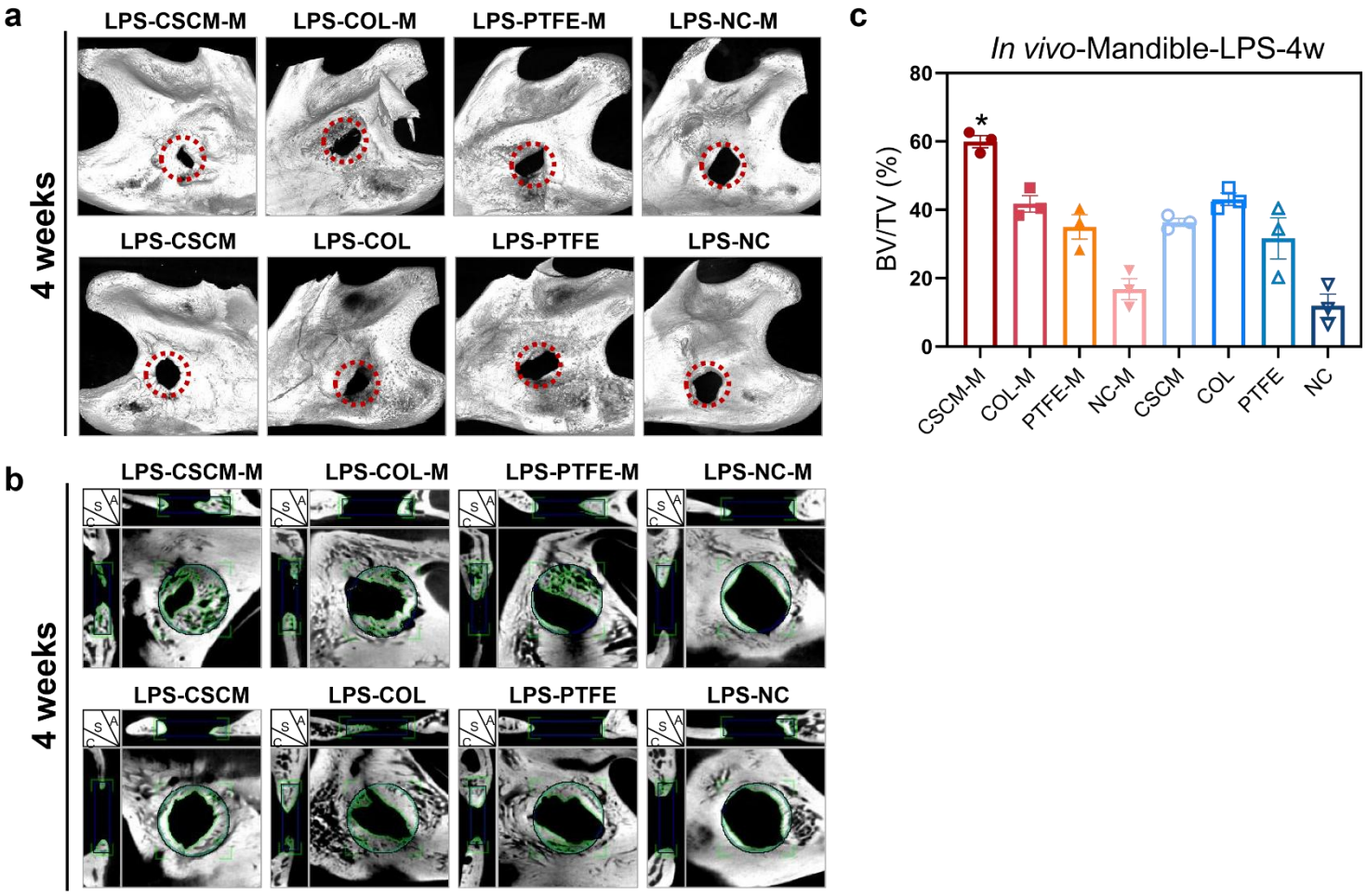


**Supplementary Fig.19 Comparison of osteogenic effects of CSCM versus commercially-available membranes in promoting bone defect repair.** The model of mandibular 3 mm critical defect combined LPS-induced systemic inflammation in rats were used in this study. **a,** Three-dimensional micro-CT images of four weeks after material implantation, with and without magnetic field treatment (4 weeks). The bone defect areas were marked by a red dotted circle. **b,** Two-dimensional images of the defect areas 4 weeks after material implantation and comorbid model preparation. The bone defect areas were marked by circles or rectangles. S=Sagittal plane, C=Coronal plane, A=Cross section. **c,** Quantitative statistics of the ratio of new bone volume to total volume (BV/TV). *n*=3 rats for per group; mean±SEM. *P<0.05, one-way ANOVA. Source data are provided as a Source Data file.

**Table S1 Osteogenesis efficiency and material morphology of the referenced materials**

| Material name | Morphology | Stimulus type | Data form | Osteogenesis efficiency (%) | References |
|---|---|---|---|---|---|
| BTO NP /P(VDF-TrFE) | membrane | Electroactive | BV/TV | 56 (12 w); 50 (4 w) | (1) |
| BFO+ | membrane | Electroactive | BV/TV | 54 (8 w) | (2) |
| P(VDF-TrFE) | membrane | Electroactive | BV/TV | 52 (8 w) | (3) |
| KNN | ceramic | Electroactive | BV | 1.2 $mm^3$ | (4) |
| AGCP | gel | Electroactive | BV/TV | 53 (12 w) | (5) |
| Actuator | scaffold | Electroactive | Area | 40 (4 w) | (6) |
| PVDF-TrFE/BT | scaffold | Electroactive | BV/TV | 20 (4 w) | (7) |
| GO-CMC | scaffold | Electroactive | BV/TV | 30± | (8) |
| nHA/GO/CS+ | scaffold | Photothermal | BV/TV | 20 (8 w) | (9) |
| 5BCN@AKT | scaffold | Photothermal | BV/TV | 58.2 (8 w) | (10) |
| $GdPO_4$/CS/$Fe_3O_4$ | scaffold | Photothermal | BV/TV | 61.23 (12w) | (11) |
| TCP-PDLLA-5LB | scaffold | Photothermal | Area | 35 (8 w) | (12) |
| BP-$SrCl_2$/PLGA +Laser | microsphere | Photothermal | BV/TV | 38 (8 w) | (13) |
| BPs@PLGA+NIR | membrane | Photothermal | BV/TV | 29.57 (10 w) | (14) |
| ACS+NSD-BMP+ US | liposome | Sonodynamic | BV/TV | 20 (4 w) | (15) |
| LIPUS+$BaTiO_3$/pT i | scaffold | Sonodynamic | BV/TV | 30 (12 w) | (16) |
| α-TCP/CS/$Fe_3O_4$/G O | cement | Magnetic | BV/TV | 18 (8 w) | (17) |
| AKT-$Fe_3O_4$-$CaO_2$ | scaffold | Magnetic | BV/TV | 12 (8 w) | (18) |
| BMSC-$Fe_3O_4$-SMF-Exos | particles | Magnetic | BV/TV | 49 (12 w) | (19) |
| Magnetic scaffold B | scaffold | Magnetic | Area | 36.23 (8 w) | (20) |
| Iron oxide core coated with PEI-B | particles | Magnetic | Healing | 43 (8 w) | (21) |
| CS/Col/$Fe_3O_4$ /nHAP | scaffold | Magnetic | BV/TV | 23 (8 w) | (22) |
| CFO/P(VDF-TrFE) -E/M | membrane | Magneto-electric | BV/TV | 52.41 (8 w) | (23) |
| CFO@BTO/P(VD F-TrFE)-M | membrane | Magneto-electric | BV/TV | 69.33 (8 w) | Our work |

**Table S1. Studies using animal experiments to assess *in vivo* osteogenesis efficiency were included.**

Based on a natural bone healing time of 12 weeks, this table only included *in vivo* studies that lasted no longer than 12 weeks to compare the efficiency of biomaterials. All included biomaterials and the results of CSCM-M under both conventional and co-morbidity conditions were concluded in Fig 1a.

**Table S2 Osteogenesis efficiency (%) at 4 weeks post-implantation**

| Group Name | Bone defect | Bone defect with Co-morbidity |
|---|---|---|
| CSCM-M | 56.05 | 52.08 |
| CCM-M | 40.76 | 33.67 |
| CSCM | 37.85 | 29.63 |
| CCM | 31.78 | 22.99 |

## Supplementary References


1 Zhang, X. *et al.* Nanocomposite Membranes Enhance Bone Regeneration Through Restoring Physiological Electric Microenvironment. *ACS Nano* **10**, 7279-7286, doi:10.1021/acsnano.6b02247 (2016).

2 Liu, Y. *et al.* Built-In Electric Fields Dramatically Induce Enhancement of Osseointegration. *Advanced Functional Materials* **27**, doi:10.1002/adfm.201703771 (2017).

3 Zhang, C. *et al.* Modulating Surface Potential by Controlling the beta Phase Content in Poly(vinylidene fluoridetrifluoroethylene) Membranes Enhances Bone Regeneration. *Adv Healthc Mater* **7**, e1701466, doi:10.1002/adhm.201701466 (2018).

4 Yu, P. *et al.* Bone-Inspired Spatially Specific Piezoelectricity Induces Bone Regeneration. *Theranostics* **7**, 3387-3397, doi:10.7150/thno.19748 (2017).

5 Kapat, K. *et al.* Osteochondral Defects Healing Using Extracellular Matrix Mimetic Phosphate/Sulfate Decorated GAGs-Agarose Gel and Quantitative Micro-CT Evaluation. *ACS Biomater Sci Eng* **5**, 149-164, doi:10.1021/acsbiomaterials.8b00253 (2019).

6 Reis, J. *et al.* A new piezoelectric actuator induces bone formation *in vivo*: a preliminary study. *J Biomed Biotechnol* **2012**, 613403, doi:10.1155/2012/613403 (2012).

7 Freitas, G. P. *et al.* Potential of Osteoblastic Cells Derived from Bone Marrow and Adipose Tissue Associated with a Polymer/Ceramic Composite to Repair Bone Tissue. *Calcif Tissue Int* **101**, 312-320, doi:10.1007/s00223-017-0282-3 (2017).

8 Ruan, J. *et al.* Enhanced Physiochemical and Mechanical Performance of Chitosan-Grafted Graphene Oxide for Superior Osteoinductivity. *Advanced Functional Materials* **26**, 1085-1097, doi:10.1002/adfm.201504141 (2016).

9 Ma, L. *et al.* A novel photothermally controlled multifunctional scaffold for clinical treatment of osteosarcoma and tissue regeneration. *Materials Today* **36**, 48-62, doi:10.1016/j.mattod.2019.12.005 (2020).

10 Zhao, C., Shen, A., Zhang, L., Lin, K. & Wang, X. Borocarbonitrides nanosheets engineered 3D-printed scaffolds for integrated strategy of osteosarcoma therapy and bone regeneration. *Chemical Engineering Journal* **401**, doi:10.1016/j.cej.2020.125989 (2020).

11 Zhao, P.-P. *et al.* Ordered arrangement of hydrated $GdPO_4$ nanorods in magnetic chitosan matrix promotes tumor photothermal therapy and bone regeneration against breast cancer bone metastases. *Chemical Engineering Journal* **381**, doi:10.1016/j.cej.2019.122694 (2020).

12 Dang, W. *et al.* LaB6 surface chemistry-reinforced scaffolds for treating bone tumors and bone defects. *Applied Materials Today* **16**, 42-55, doi:10.1016/j.apmt.2019.04.015 (2019).

13 Wang, X. *et al.* Near-infrared light-triggered drug delivery system based on black phosphorus for *in vivo* bone regeneration. *Biomaterials* **179**, 164-174, doi:10.1016/j.biomaterials.2018.06.039 (2018).

14 Tong, L. *et al.* Near-infrared light control of bone regeneration with biodegradable photothermal osteoimplant. *Biomaterials* **193**, 1-11, doi:10.1016/j.biomaterials.2018.12.008 (2019).

15 Crasto, G. J. *et al.* Controlled bone formation using ultrasound-triggered release of BMP-2 from liposomes. *J. Control. Release* **243**, 99-108, doi:10.1016/j.jconrel.2016.09.032 (2016).

16 Fan, B. *et al.* Electroactive barium titanate coated titanium scaffold improves osteogenesis and osseointegration with low-intensity pulsed ultrasound for large segmental bone defects.

*Bioactive materials* **5**, 1087-1101, doi:10.1016/j.bioactmat.2020.07.001 (2020).

17 Yan, F. *et al.* Biphasic Injectable Bone Cement with $Fe_3O_4$/GO Nanocomposites for the Minimally Invasive Treatment of Tumor-Induced Bone Destruction. *ACS Biomater Sci Eng* **5**, 5833-5843, doi:10.1021/acsbiomaterials.9b00472 (2019).

18 Dong, S., Chen, Y., Yu, L., Lin, K. & Wang, X. Magnetic Hyperthermia–Synergistic $H_2O_2$ Self-Sufficient Catalytic Suppression of Osteosarcoma with Enhanced Bone-Regeneration Bioactivity by 3D-Printing Composite Scaffolds. *Advanced Functional Materials* **30**, doi:10.1002/adfm.201907071 (2019).

19 Wu, D. *et al.* Bone mesenchymal stem cells stimulation by magnetic nanoparticles and a static magnetic field: release of exosomal miR-1260a improves osteogenesis and angiogenesis. *J Nanobiotechnology* **19**, 209, doi:10.1186/s12951-021-00958-6 (2021).

20 Panseri, S. *et al.* Modifying bone scaffold architecture *in vivo* with permanent magnets to facilitate fixation of magnetic scaffolds. *Bone* **56**, 432-439, doi:10.1016/j.bone.2013.07.015 (2013).

21 Brett, E. *et al.* Magnetic Nanoparticle-Based Upregulation of B-Cell Lymphoma 2 Enhances Bone Regeneration. *Stem Cells Transl Med* **6**, 151-160, doi:10.5966/sctm.2016-0051 (2017).

22 Zhao, Y. *et al.* Magnetic bioinspired micro/nanostructured composite scaffold for bone regeneration. *Colloids Surf B Biointerfaces* **174**, 70-79, doi:10.1016/j.colsurfb.2018.11.003 (2019).

23 Liu, W. *et al.* Remote Tuning of Built‐In Magnetoelectric Microenvironment to Promote Bone Regeneration by Modulating Cellular Exposure to Arginylglycylaspartic Acid Peptide. *Advanced Functional Materials* **31**, 2006226, doi:10.1002/adfm.202006226 (2020).